Structure of Core Domain of Fibril-Forming PHF/Tau Fragments

Hideyo Inouye,* Deepak Sharma,* Warren J. Goux,† and Daniel A. Kirschner*
*Boston College, Biology Department, Chestnut Hill, Massachusetts; and †Department of Chemistry, The University of Texas at Dallas, Richardson, Texas

ABSTRACT Short peptide sequences within the microtubule binding domain of the protein Tau are proposed to be core nucleation sites for formation of amyloid fibrils displaying the paired helical filament (PHF) morphology characteristic of neurofibrillary tangles. To study the structure of these proposed nucleation sites, we analyzed the x-ray diffraction patterns from the assemblies formed by a variety of PHF/tau-related peptide constructs containing the motifs VQIINK (PHF6*) in the second repeat and VQIVYK (PHF6) in the third repeat of tau. Peptides included: tripeptide acetyl-VYK-amide (AcVYK), tetrapeptide acetyl-IVYK-amide (AcPHF4), hexapeptide acetyl-VQIVYK-amide (AcPHF6), and acetyl-GKVQIINKLDLSNVQKDNIKHGSVQIVYKPVDLSKVT-amide (AcTR4). All diffraction patterns showed reflections at spacings of 4.7 Å, 3.8 Å, and ~8–10 Å, which are characteristic of an orthogonal unit cell of β-sheets having dimensions $a = 9.4$ Å, $b = 6.6$ Å, and $c = \sim$8–10 Å (where a, b, and c are the lattice constants in the H-bonding, chain, and intersheet directions). The sharp 4.7 Å reflections indicate that the β-crystallites are likely to be elongated along the H-bonding direction and in a cross-β conformation. The assembly of the AcTR4 peptide, which contains both the PHF6 and PHF6* motifs, consisted of twisted sheets, as indicated by a unique fanning of the diffuse equatorial scattering and meridional accentuation of the (210) reflection at 3.8 Å spacing. The diffraction data for AcVYK, AcPHF4, and AcPHF6 all were consistent with ~50 Å-wide tubular assemblies having double-walls, where β-strands constitute the walls. In this structure, the peptides are H-bonded together in the fiber direction, and the intersheet direction is radial. The positive-charged lysine residues face the aqueous medium, and tyrosine-tyrosine aromatic interactions stabilize the intersheet (double-wall) layers. This particular contact, which may be involved in PHF fibril formation, is proposed here as a possible aromatic target for anti-tauopathy drugs.

INTRODUCTION

Tau is a microtubule binding protein that is proposed to play a role in maintaining cytoskeletal superstructure by acting as a spacer between microtubules (1,2). In Alzheimer's disease, the ordered cytoskeleton consisting of microtubules, tau, and intermediate filaments is destroyed, resulting in a precipitation of neurofibrillary tangles in the cytoplasm. Major structural components are paired helical filaments (PHF) and straight filaments. PHF are 8–20 nm wide and have a cross-over spacing of 80 nm (3), and straight filaments are 15-nm wide. As a major constituent of PHF, hyperphosphorylated tau protein may play a crucial role in dissociating tau and tubulin (4); however, its role in PHF fibril formation is not clear (5,6). It has been hypothesized that the short hexapeptide motifs in the second and third repeat of tau VQIINK (PHF6* in R2) and VQIVYK (PHF6 in R3) interact to form the unique twisted-ribbonlike morphology of PHF (7,8). The tripeptide VYK is minimally sufficient for fibril formation (9); and mixing VYK with PHF6 gives PHF-like twisted filaments (9). That β-sheet structure is involved in PHF formation (10) is shown by x-ray diffraction, electron microscopic, ESR, and spectroscopic studies of native filaments from brain, mutant constructs, and short peptides including the core domain (7–9,11,12). By contrast, α-helical or mixtures of α-helical, β-turn, and β-sheet conformations have been reported for aggregated tau from brain samples of AD patients (13,14).

Although results with peptides suggest that the interaction between VYK residues in multiple segments of tau may act in concert to initiate the formation of cross-β tau (9), the structures of short core peptides and assemblies of longer peptides containing two motif sequences have not been elucidated. Because PHF is thought to be cytotoxic for neurons and could conceivably serve as a target for drugs such as aromatic anthraquinones (15) and phenothiazines, polyphenols, and porphyrins (16), structural information on PHF-related assemblies could be beneficial for rationale drug design. This article reports a detailed analysis of the x-ray diffraction patterns that we recently reported for a variety of PHF/tau-related peptides including acetyl-VYK-amide (AcVTK), acetyl-IVYK-amide (AcPHF4), and acetyl-VQIVYK-amide (PHF6) (9), and a longer peptide construct containing both PHF6* and PHF6, i.e., acetyl-GKVQIINKLDLSNVQKDNIKHGSVQIVYKPVDLSKVT-amide (AcTR4). Our analysis shows that AcTR4 peptide containing two motifs gave a twisted fibrillar structure, whereas AcVYK, AcPHF4, and AcPHF6 peptides form ~50 Å-wide, double-wall tubular cylinders. We propose an atomic model, which indicates that PHF formation is likely initiated by the interaction between aromatic tyrosine residues. Thus, inhibitory mechanisms that involve the targeting by compounds of the aromatic core domain may inhibit nucleation of PHF.

Submitted July 7, 2005, and accepted for publication November 14, 2005.

Address reprint requests to Daniel A. Kirschner, Tel.: 617-552-0211; E-mail: kirschnd@bc.edu.

0006-3495/06/03/1774/16 $2.00

doi: 10.1529/biophysj.105.070136

MATERIALS AND METHODS

Peptides, sample preparation, and x-ray diffraction

Diffraction patterns from the tri-, tetra-, and hexapeptides were recently described, as were the source and preparation of those peptides (9). Additionally, we used peptide AcTR4 (acetyl-GKVQIINKLDLSNVQKD-NIKHGKVQIVYKPVDLSKVT-amide which, based on a pairwise sequence comparison (17) http://pir.georgetown.edu/pirwww/search/pairwise.html), contains two core domains in the human tau sequence 272–318 (SWISS-PROT Database, Accession #P10636-8), as shown here:

```
             250        260        270        280        290        300
              |          |          |          |          |          |
tau    LQTAPVPMPDLKNVKSKIGSTENLKHQPGGGKVQIINKKLDLSNVQSKCGSKDNIKHVP
                                     :::::::: :::::::     ::::::
TR4                                  GKVQIINK-LDLSNVQ-----KDNIKH--

             310        320        330        340        350        360
              |          |          |          |          |          |
tau    GGGSVQIVYKPVDLSKVTSKCGSLGNIHHKPGGGQVEVKSEKLDFKDRVQSKIGSLDNIT
         ::::::::::::::::
TR4    --GSVQIVYKPVDLSKVT
```

The AcTR4 peptide was purchased from the Core Lab Facility, Tufts University, Department of Physiology (Boston, MA). After confirmation of its sequence by MALDI-TOF mass spectrometry, AcTR4 in lyophilized form was refrigerated until further use. AcTR4 was analyzed under different conditions: lyophilized (L), vapor-hydrated (VH), and solubilized then dried (S/D), as previously described for the other peptides (9), where the experimental conditions for obtaining the diffraction patterns are also detailed.

Sequence analysis

The sequence-specific patterns for the different physical-chemical attributes of the peptides (e.g., hydrophobicity, polarity, charge, side-chain size) were analyzed by methods including Fourier-transform and averaging (18). The secondary structures (a, α-helix; b, β-strand; c, coil; and t, turn) were predicted according to Garnier's method with a zero decision constant (19). The number density of the specific amino acids was calculated as a function of distance from the center of gravity of the molecule.

Transmission electron microscopy (TEM)

All peptides were dissolved in either 5 mM or 20 mM 3-[N-morpholino]-propanesulfonic acid (MOPS) buffer, pH 7.2 The final concentration of the peptide monomer was between 0.1 and 1 mg/mL. Samples, most of which were aged at least two days at room temperature (~21°C) before TEM, were prepared by floating a formvar carbon-coated copper grid on a 10-μL drop of the sample for 10 min. The sample was then negative-stained for 2 min with 2% uranyl acetate, rinsed once with deionized water, and dried by wicking. A JEOL 1200 EX scope interfaced to a digital camera was used to examine samples (JEOL, Peabody, MA).

X-ray data reduction

Quantitation of the observed intensity, application of the Lorentz and polarization factors, calculation of the structure amplitudes, and determination of lattice constants and their indices were all carried out using methods previously elaborated (20,21).

Fourier synthesis and model building

The procedure of Fourier synthesis for fiber and powder diffraction, which is based on choosing initial phase models from geometric structures or known atomic models, has been detailed (20,22). The cylindrical and twisted sheet structures described here were constructed as described (23,24). To build atomic models of the peptides that were N-terminal-acetylated and C-terminal-amidated, first a polyalanine peptide in the β-conformation was built by Swiss-PDB Viewer (25), next the N- and Cβ-atoms of the N-terminal alanine residue were removed (where the α-carbon of the alanine residue refers to the position of CH_3 in the acetyl residue), and then the C-terminal OH group of $-$COOH was created and the OH group was replaced by an NH_2 group. As previously, the molecular models were displayed and manipulated using MOLSCRIPT (26), XtalView (27), RasMol (28), and Swiss-PDB Viewer.

Predicted transforms for different geometric models

The initial phase models that were tested against the equatorial x-ray data up to ~5 Å spacing were single-wall and double-wall tubes, a solid cylinder, and a plate. These simple geometric models have been tested previously at this resolution for amyloid fibrils (20,29–32). The analytical form for the structure factors for these models are given below, and the residuals R between the observed and calculated structure amplitudes for the observed Bragg peaks ($R_{\text{obs-amp}}$) or scattering intensities of the continuous curves ($R_{\text{tot-int}}$) (20) were calculated by systematically changing the parameters defining the model. The best parameters were those that gave a minimum R-factor.

Tubular structures

For a cylindrically symmetric structure with no variation along the fiber axis, i.e., the z axis, the electron density distribution can be given in the cylindrical coordinates as $\rho(r,\phi,z) = \rho(r)$. Thus, the Fourier-transform of $\rho(r)$ is given by

$$F(R) = \int_0^\infty 2\pi r\rho(r)J_0(2\pi rR)dr. \quad (1)$$

Double-wall cylinder

For a double-wall cylinder having inner and outer radii r_i and r_o, $\rho(r) = 1$ at $r = r_i$ and $r = r_o$. Therefore,

$$F(R) = 2\pi[r_iJ_0(2\pi r_iR) + r_oJ_0(2\pi r_oR)]. \quad (2)$$

For a cylinder having a single wall, either of the terms in Eq. 2 may be deleted.

Solid cylinder

The structure factor can be written as

$$F(R) = rJ_1(2\pi rR)/R. \quad (3)$$

Double thin plates

For a pair of lines having lengths b_0 and separated by a_t, the intensity is

$$I(X, Y) = 2[b_0 \sin c(\pi b_0 Y)]^2[1 + \cos(2\pi a_t X)]. \quad (4)$$

Given R as the amplitude of the vector in the radial component of the cylindrical coordinates, then the spherically averaged intensity $I_s(R) = \sum\sum I(X,Y)/R^2$ where $R^2 = X^2 + Y^2$.

For some structures studied here, the interference function is 1, and the observed scattering then arises from the structure amplitudes. The diffraction patterns were either powder- or fiberlike, where the Bragg reflections are spherically or cylindrically averaged. The assignment of the Miller indices to the observed reflections and extraction of the structure amplitudes, therefore, were not straightforward, but model-dependent (20). Different geometric or atomic models were tested against the observed diffraction intensity, and then the best parameters were searched. The goodness-of-fit (R-factor) between the observed and calculated amplitudes or intensities is a quantitative assessment of the solution, and is given either by $R_{\text{obs-amp}}$ or by $R_{\text{tot-int}}$ according to

$$R_{\text{obs-amp}} = \frac{\sum||F_{\text{obs}}| - |F_{\text{calc}}||}{\sum|F_{\text{obs}}|} \quad \text{and} \quad R_{\text{tot-int}} = \frac{\sum|I_{\text{obs}} - I_{\text{calc}}|}{\sum I_{\text{obs}}}.$$

Measurement of crystallinity

To assess the amount of peptide in the assembly as a fraction of the total peptide volume, the crystallinity was measured. The observed intensity (I_{obs}) is composed of the intensities from peptide (I_p) and from the blank (i.e., capillary tube and bulk medium, or I_c)—i.e., $I_{\text{obs}} = I_p + I_c$.

The diffracting power P arising from the peptides is defined by

$$P = \int I_p(\vec{R})d\vec{R},$$

where R is the reciprocal coordinate. Parseval's equation relates this to the electron density distribution by

$$P = \int \rho_p(\vec{r})^2 d\vec{r}.$$

From the average electron density $\langle\rho_p\rangle$ and the total volume of the scattering object V_p, then $P = V_p\langle\rho_p\rangle^2$. The experiment indicates that P is the sum of the assembled peptides (A) and the disordered amorphous peptides (B). The volume and electron density of an individual part is written as

$$V_p\langle\rho\rangle^2 = V_A\langle\rho_A\rangle^2 + V_B\langle\rho_B\rangle^2,$$

where A was measured as the integral area under the observed intensity curve after background subtraction, and the area under the background curve above the intensity from the blank is denoted here as B. The capillary tube gave a broad maximum at 0.25 Å^{-1}, and the intensity was nearly flat between 0.05 and 0.2 Å^{-1}. We assumed that the flat blank intensity curve crossed the intensity minimum of the observed intensity within the region of 0.05–0.2 Å^{-1}. Fitting the background intensity minima by a polynomial, we obtained the I_B intensity by subtracting the blank intensity from the background intensity. The volume fraction of the assembled peptides, therefore, was calculated according to $I_A/(I_A+I_B)$. Note these intensities refer to the squared structure amplitudes F^2. When the intensity from the two-dimensional detector was measured along the radial direction R, F^2 is related to the observed intensity multiplied by R^2 for powder diffraction; and when the intensity was measured along the layer line R, F^2 is related to the observed intensity multiplied by R for fiber diffraction.

ANALYSIS AND RESULTS

Ultrastructure of tau-related peptides

Examination by TEM of all of the shorter peptides, which has been reported previously (9), demonstrated abundant filaments in water or MOPS buffer at pH 7.2. For AcTR4, typical amyloidlike filaments were also observed after dissolving the lyophilized peptide in buffer (Fig. 1). This result is consistent with FTIR data showing the presence of β-sheet (data not shown).

Overview of x-ray patterns: core domains show β-sheet folding

All diffraction patterns of the PHF/tau-related peptides from the three different preparations (lyophilized, vapor-hydrated, and solubilized/dried) showed reflections characteristic of orthogonal unit cells of β-sheets: i.e., a sharp reflection at ~4.7 Å spacing, and reflections at ~8–10 Å and 3.8 Å spacing (Fig. 2) (9). The unit cell dimensions along the H-bonding, chain, and intersheet axes were $a = 9.4$ Å, $b = 6.6$ Å, and $c =$ ~8–10 Å (Fig. 2), and the corresponding Miller indices were (200) for 4.7 Å, (210) for 3.8 Å, and (001) for 8–10 Å. The lyophilized and vapor-hydrated samples of peptides AcVYK, AcPHF4, AcPHF6, and AcTR4 (data not shown), and the lyophilized and solubilized/dried AcVYK (Fig. 2), showed spherically averaged intensity, indicating that the scattering objects in these assemblies were oriented randomly. By contrast, the intensity in the patterns from solubilized/dried AcPHF6 and AcTR4 was cylindrically averaged, consistent with the fiber axis being along the direction of the 4.7 Å reflection. With the meridional axis along the H-bonding direction, the equatorial scatter was interpreted as arising from the packing of fibers. The ~10 Å, intersheet (001) reflection, therefore, was on the equator, and the (210) reflection at 3.8 Å spacing was off-meridional on

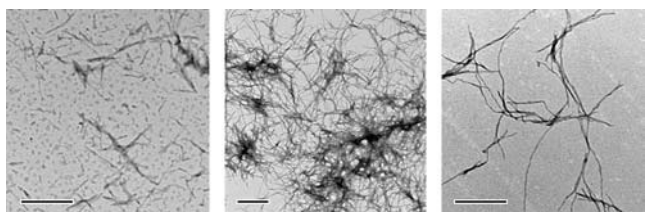

FIGURE 1 Electron micrographs from AcTR4. (*Left*) Sample immediately after mixing the peptide in 20 mM MOPS buffer reveals a mixture of many short or indistinct fibers as well as longer assemblies. (*Middle* and *right*) After two days' incubation, the samples show numerous well-formed fibers. Scale bars: 5000 Å.

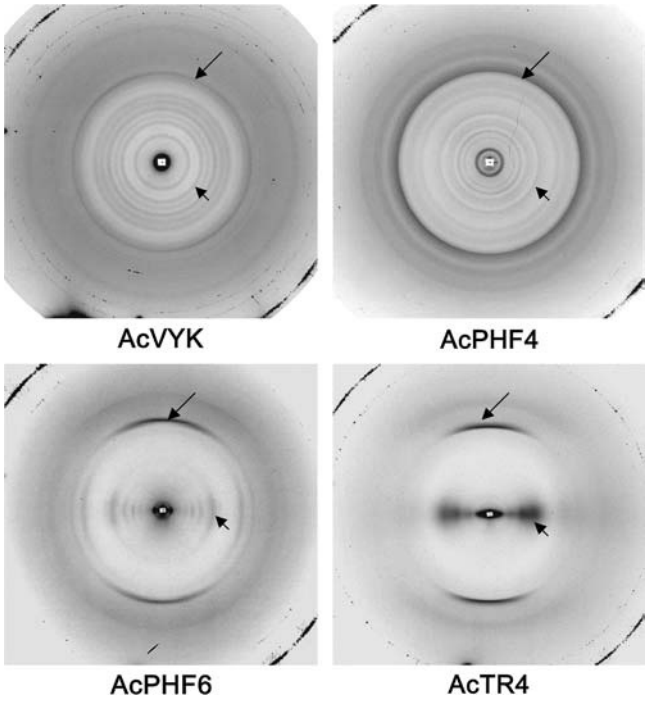

FIGURE 2 X-ray diffraction patterns of solubilized/dried AcVYK, AcPHF4, AcPHF6, and AcTR4 peptides. The brightness and contrast have been adjusted to show clearly the positions of the observed reflections, including the off-meridional and meridional accentuation of the 3.8 Å reflection for AcPHF6 and AcTR4. The long arrows indicate the position of the H-bonding reflection at ~4.7 Å spacing, and the short arrows indicate the approximate positions of the intensity maxima corresponding to intersheet distances of ~8–10 Å.

the 4.7 Å-layer line for AcPHF6. These reflections indicate that the β-chains were running nearly normal to the fiber direction, i.e., in the cross-β-conformation. The 3.8 Å reflection of AcTR4, however, was accentuated on the meridian, indicating that the tilting of the β-chains was likely related to twisting of the fibril (Fig. 2). Because the shorter peptides gave spherically averaged powder diffraction rather than fiber diffraction patterns, the cylindrical axis (i.e., fibril direction) could not be determined experimentally. The sharpness of the 4.7 Å reflection indicated that the coherent domain size along the 4.7 Å H-bonding direction was large. The scattering object, therefore, was elongated along the H-bonding direction in the same way as in cross-β-structures.

Broadening of Bragg peaks arises from a decreasing coherent domain size and increasing lattice disorder (20). The integral width of the intersheet reflection at ~8–10 Å showed a coherent domain size of ~20 Å for all vapor-hydrated peptides, indicating that water disordered the arrangement of the β-sheets along the intersheet direction. Lyophilized peptides AcVYK and AcPHF4 showed coherent domain sizes of ~40 Å, whereas the slightly longer peptide AcPHF6 and the substantially longer AcTR4 gave domains approximately half the size. Solubilized/dried samples of AcVYK and AcPHF4 assemblies gave much sharper reflections typical of crystalline lattices. After solubilization/drying, the intersheet reflection from AcPHF6 was sharper than that of the lyophilized sample. Peptide AcTR4 samples in all states gave ~20 Å-wide domains which are characteristic for the thickness of a pair of β-sheets.

The volume fraction of peptide that was in the assembly was evaluated from measurement of the crystallinity using data in the region between 0.05 and 0.20 $Å^{-1}$ (Table 1). For the short peptides, the crystallinity of the lyophilized and solubilized/dried samples was similar, as might be expected for samples containing little if any water, and the vapor-hydrated sample showed the least amount of crystallinity. For TR4, by contrast, the greatest amount of crystallinity was shown by the assemblies that had been solubilized then dried.

AcVYK assembly

Broad intensity maxima at spacings 27 Å, 14 Å, 9.1 Å, 6.7 Å, 5.8 Å, 4.6 Å, and 3.9 Å were apparent in densitometer tracings of the pattern from lyophilized AcVYK (Fig. 2 *A*). The maxima near ~10 Å were similar to the ones for Aβ1–40 (31,33). The strong peak at ~4.6 Å and the shoulder at ~3.9 Å likely arise from the (200) and (210) reflections of a β-sheet orthogonal unit cell as described above (20). An apparent one-dimensional lattice having a 28 Å-period accounted for the indexing of the first five low-angle reflections, indicating that these peaks likely correspond to the maxima from the J_0 Bessel term $aR = 1.11$, where $R = (28\ Å)^{-1}$ and a, the separation between the structural units, was estimated to be 31 Å. If the reflection at 9.1 Å spacing is indexed as the (001) of the β-sheet assembly (where the c axis is parallel to the intersheet direction), then for a coaxial cylinder model the inter-wall separation is 9.1 Å × 1.11 = 10.1 Å. The inner and outer radii r_i and r_o of the cylinders were determined by searching systematically for the minimum R-factor (i.e., $R_{\text{tot-int}} = \sum|I_{\text{obs}} - I_{\text{cal}}|/\sum I_{\text{obs}}$) and found to be 10.2 Å and 18.8 Å, respectively (Fig. 3 *C*). By comparison, a solid cylinder model and a single tubular model gave poorer fits to the observed intensity. The pair of intensity maxima at 9.0 Å and 5.8 Å were also evident for the vapor-hydrated tripeptide AcVYK (Fig. 3 *A*), and therefore likely arise from coaxial cylinders having similar radii.

TABLE 1 Crystallinity of the samples for x-ray diffraction

Peptide	Lyophilized	Vapor-hydrated	Solubilized/dried
AcVYK	0.68	0.12	0.47
AcPHF4	0.52	0.43	0.65
AcPHF6	0.40	0.16	0.51
AcTR4	0.19	0.10	0.80

The tabulated values indicate the fractional amount of ordered domain, as determined for the fibrillar form of the assembly as indicated by the sharp H-bonding reflection (at 4.7 Å) and by electron microscopy for the shorter peptides (Goux et al. (9)) and for AcTR4 (Fig. 1).

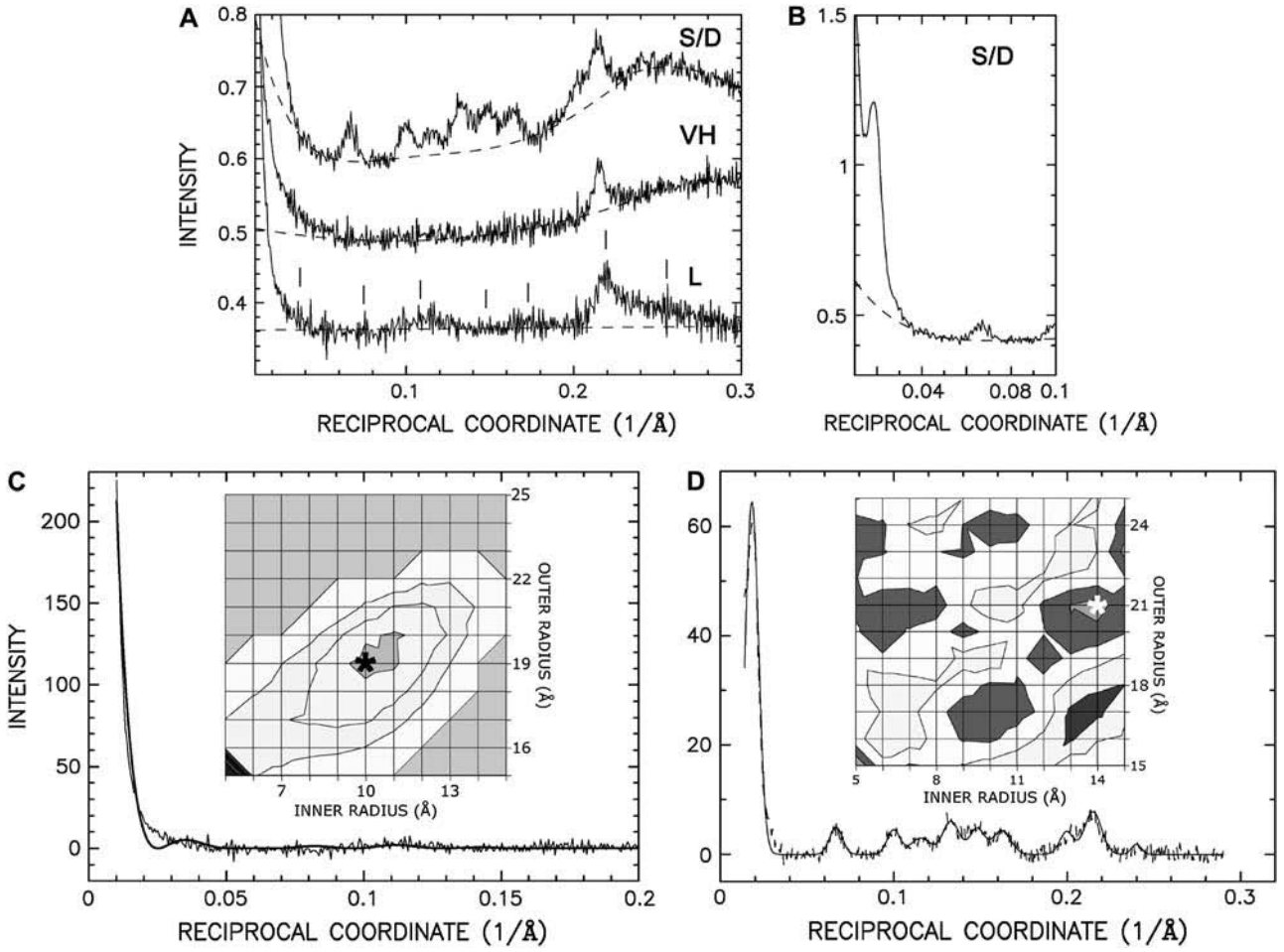

FIGURE 3 X-ray diffraction and analysis from PHF/tau tripeptide AcVYK. (*A*) The intensity distributions for different sample preparations as a function of reciprocal coordinate for solubilized/dried (*S/D*), vapor-hydrated (*VH*), and lyophilized (*L*) samples. The intensities are displaced vertically for clarity. The intensity was measured from linear scans, converted to the optical density scale, and plotted as a function of reciprocal coordinate in $(\text{Å})^{-1}$. The intensity was not corrected for the Lorentz type and polarization factors (LP correction). The vertical bars indicate the positions of the intensity maxima in the lyophilized sample. (*B*) Intensity distribution showing the low-angle peak for the solubilized/dried sample. The background curve (*dashed line*) was derived by a polynomial fit. (*C*) Analysis of diffraction from lyophilized AcVYK. The observed intensity (*thinner line*) and calculated one based on a double-wall cylinder of 10 Å inner and 19 Å outer radius (*thicker line*) were both normalized, so that the area under the curve was unity. The LP correction was applied to the calculated data. (*Inset*) Dependence of *R*-factor on different inner and outer radii. The minimum $R_{\text{obs-amp}}$ (*) of 0.45 was obtained at inner and outer radii 10 Å and 19 Å. (The boundary including the minimum $R_{\text{obs-amp}}$ was in the range of 0.44–0.455 and the subsequent boundaries were drawn every 0.015.) (*D*) Analysis of diffraction from solubilized/dried AcVYK after background subtraction. The observed data (*dashed line*) and one fit by multiple Gaussian curves (*solid line*), were normalized as above. (*Inset*) Dependence of *R*-factor on different inner and outer radii (see above). The minimum *R*-factor was 0.19 at 14 Å and 21 Å inner and outer radii. (The boundary including the minimum $R_{\text{obs-amp}}$ was in the range of 0.1–0.3, and the subsequent boundaries were drawn at every 0.2.)

The assemblies formed by the solubilized/dried tripeptide gave many concentric rings to ~5 Å spacing and was indexed by a two-dimensional hexagonal lattice of 63.7 Å unit cell (Fig. 3, *A* and *B*; Table 2). The very strong low-angle reflection at 55 Å was indexed as (10). Optimization of the inner and outer radii for a coaxial cylinder model was performed as above, and gave values of 14.0 Å and 20.8 Å, respectively (Fig. 3 *D*), which were 2–4 Å larger than those for the lyophilized sample. Because a tubular form of the β-sheet structure was apparently already present in the lyophilized state, then the solubilization and drying resulted in formation of an hexagonal arrangement of the tubular assemblies.

To fit atomic models of AcVYK to the electron density maps that were derived by using phases from a tubular model and the observed amplitudes (Fig. 4), the lysine residues were positioned facing the aqueous medium, and the tyrosine residues were placed in the intersheet space. The positive-charge of the lysines is presumably countered by anions. Trial and error was used to give physically plausible molecular packing and resulted in seven tripeptide molecules arrayed at radius 14 Å and nine molecules at radius 21 Å. The inner and outer walls of the coaxial cylinder were assumed to trace out a helix, as in the case for the waterfilled, polyglutamine nanotube (32).

TABLE 2 Observed and calculated Bragg spacings for powder patterns from AcVYK and AcPHF4 assemblies after solubilization and drying

AcVYK			AcPHF4		
Miller index (kl)	d_{obs}	d_{calc}	Miller index (kl)	d_{obs}	d_{calc}
10	55.2	55.2	10	60.6	60.1
13	15.0	15.3	11	34.2	34.7
24	10.0	10.4	20	30.1	30.1
16	8.66	8.41	12	22.3	22.7
26	7.52	7.65	30	20.0	20.0
27	6.76	6.74	13	16.7	16.7
18, 46	6.16	6.33, 6.37, 6.46	40	14.9	15.0
			23	13.8	13.8
			14	13.1	13.1
			24	11.3	11.4
			15	10.7	10.8
			60	9.93	10.0
			35, 44, 70	8.37	8.59, 8.68
$R_{obs\text{-}amp}$	0.20		0.29		
b, c	63.7 Å		69.4 Å		
α	120°		120°		
r_i	14 Å		18 Å		
r_o	21 Å		28 Å		

The observed indices include (0kl), (0k-l), (0lk), (0l-k), and respective Friedel pairs. Positive integers only are shown for the Miller indices. The observed Bragg spacings were determined after fitting the scanned intensity on the equator by multiple Gaussian peak functions.

Other atomic models were also tested against the observed x-ray data to ~5 Å Bragg spacing. One model included the peptide backbone and Cβ atoms, which were extracted from the foregoing model, and another model had the tyrosine residues facing the aqueous medium. For these models, the $R_{obs\text{-}amp}$ values were calculated to be 0.39 and 0.53, respectively. Because the R-factors for the coaxial cylinder model and the model where lysine residues face the medium gave values of 0.19 and 0.53, respectively, then details of residue orientation could not be resolved by the current low-resolution data by itself.

AcPHF4 assembly

For the lyophilized tetrapeptide AcPHF4, there were intensity maxima at $(11.4\ \text{Å})^{-1}$ and $(9.3.\ \text{Å})^{-1}$ (Fig. 5, *left* and *middle*). The $(50\ \text{Å})^{-1}$ separation between these indicated that, for a model of coaxial cylinders, the separation between the coaxial walls would be $50 \times 1.11 = 55$ Å (see above). Optimizing the inner and outer radii for the double wall gave values of 18 Å and 28 Å (Fig. 5, *middle*). Other models, including a solid cylinder and a single cylinder, gave poorer R-factors.

A two-dimensional hexagonal lattice with $b = c = 69.4$ Å accounted for the many concentric rings in the x-ray pattern from the solubilized/dried peptide (Fig. 5, *right*; Table 2). The (10) reflection was weak, and the (21) reflection was very weak. Of the three different models examined, a coaxial (double-wall) cylinder gave the lowest R-factor, and the inner and outer radii were 17.8 Å and 28.0 Å. The electron density projection along the H-bonding direction, derived using phases from the model and the observed amplitudes, showed two rings, and no apparent strong peaks inside or outside the cylinder (Fig. 6).

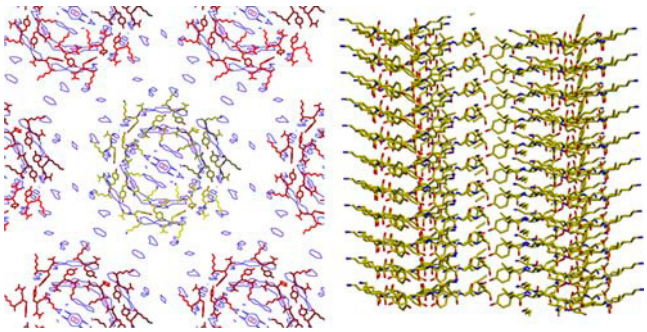

FIGURE 4 Calculated electron density map and atomic model for solubilized./dried AcVYK. (*Left*) Projection of electron density along the fiber axis was calculated using phases from a double-wall cylinder of 14 Å inner radius and 21 Å outer radius and the observed structure amplitudes. The lattice constant for the hexagonal array was 63.7 Å. The skeletal atomic model shows seven molecules at the inner radius and nine at the outer radius. The lysine residues face the inner and outer medium, whereas tyrosine residues are localized in the intersheet space. The $R_{obs\text{-}amp}$ of the atomic model was 0.53. (*Right*) View along radial direction of an individual double-wall tube. The size of the tube is shown expanded approximately twofold compared to image at left. The depth of image was adjusted to clearly show the stacking of the foreground molecules in the fibril direction. The apparent asymmetrical arrangement of peptides in this lateral view comes from the viewing perspective. The electron density map and skeletal model are XtalView representations (27). The atomic coordinates in PDB format are displayed using XtalView and Raster3D (100).

The atomic model for AcPHF4 (Fig. 6) was built in the same way as for AcVYK peptide, with the lysine residues facing the aqueous medium, and the tyrosine and isoleucine residues localized to the intersheet space. A stereochemically reasonable packing was achieved with seven molecules at the inner radius 17.5 Å and 11 molecules at the outer radius of 27.5 Å. This model gave $R_{obs\text{-}amp}$ of 0.38. Similar alternative models as for peptide AcVYK were tested against the observed x-ray intensity to ~5 Å spacing. Because the R-factors were 0.35 and 0.38, the residue orientation could not be resolved by this data.

AcPHF6 assembly

Unlike the diffraction patterns from the lyophilized tri- and tetrapeptides above, the ones from lyophilized AcPHF6 did not show multiple intensity maxima, but rather gave a single, broad reflection at 8.3 Å spacing (Fig. 7, *left* and *middle*). From its integral width $(0.044\ \text{Å}^{-1})$ and that of the direct beam $(0.0022\ \text{Å}^{-1})$, we calculated the coherent length as ~20 Å. A pair of 12 Å-long straight lines separated by 8.3 Å accounted for the observed intensity. This length corresponds to approximately four residues in a β-strand (Fig. 7, *middle*). The one-dimensional electron density distribution,

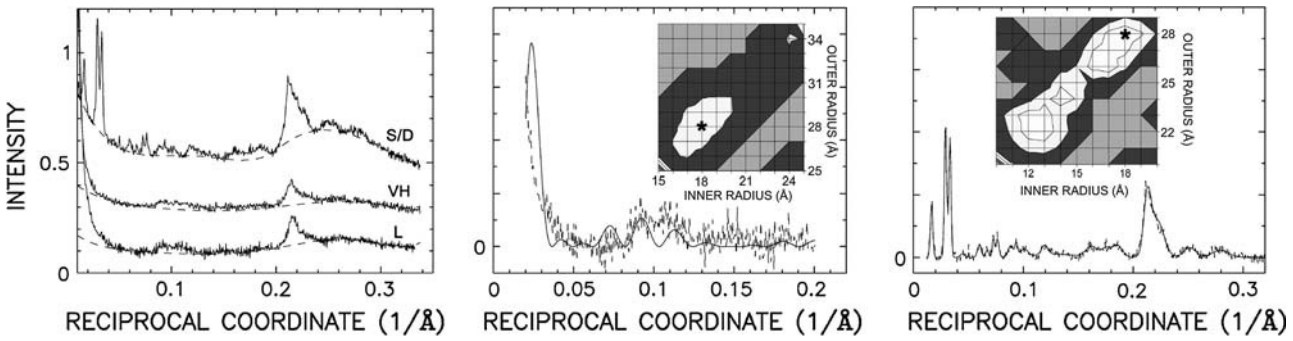

FIGURE 5 Analysis of x-ray diffraction from PHF/tau tetrapeptide AcIVYK (AcPHF4). (*Left*) The intensity distributions for solubilized/dried (*S/D*), vapor-hydrated (*VH*), and lyophilized (*L*) preparations. See Fig. 3 *A* legend for details. (*Middle*) The observed (*dashed*) and calculated (*solid*) intensity distributions for the lyophilized sample. The calculation was based on a double-wall cylinder with 18 Å inner and 28 Å outer radius. See Fig. 3 *C* for details. (*Inset*) Dependence of *R*-factor on different inner and outer radii. The minimum $R_{\text{obs-amp}}$ (*) was 0.85 at values for the inner and outer radii of 18 Å and 28 Å. (The boundary including the minimum *R*-factor was in the range of 0.8–0.9; and subsequent boundaries were drawn at every 0.1.) (*Right*) The observed (*dashed*) and Gaussian fit (*solid*) intensity distributions for solubilized/dried AcPHF4. See Fig. 3 *D* for further details. (*Inset*) Calculation carried out as described above has shown the dependence of R-factor on different inner and outer radius in Å for solubilized/dried AcPHF4 peptide. The minimum $R_{\text{obs-amp}}$ (*) was 0.29 for inner and outer radii of 18 Å and 28 Å. (The boundary including the minimum *R*-factor was in the range of 0.3–0.4, and the subsequent boundaries were drawn at every 0.1.)

calculated using the phases from the model and the observed amplitudes, showed two ~4 Å-wide peaks, which likely correspond to the β-chain backbone (Fig. 8, *right*).

The assemblies formed from the solubilized/dried hexapeptide gave an oriented fiber pattern with a sharp 4.7 Å reflection on the meridian, and a series of reflections on the equator (Fig. 7, *right*). The equatorial reflections at 95 Å and 46 Å were sharp and strong, whereas the subsequent ones were much broader and weaker. The two sharp reflections were interpreted as arising from an interference function and were indexed as (10) and (20) of an hexagonal lattice of $b = c = 107.3$ Å. The subsequent broad reflections, therefore, correspond to the structure amplitudes of a unit object. By systematically varying the inner and outer radii for a geometric model consisting of a coaxial cylinder, we searched for the minimum *R*-factor, and found the inner radius to be 13 Å and the outer to be 22 Å. As the low-resolution intensity data in this study did not resolve the orientation of the residues (see above, alternative atomic models for AcVYK, and AcPHF4), we did not derive an atomic model. On the basis of electrostatic effects on the β-sheet assembly, however, it is likely that the positive-charged lysine residues face the aqueous medium in the same way as in the shorter peptides.

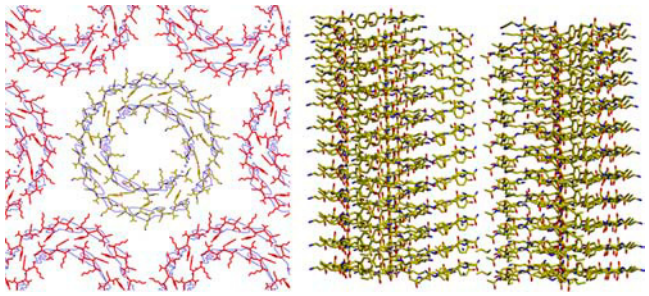

FIGURE 6 Calculated electron density map and atomic model for solubilized/dried AcPHF4. (*Left*) Electron density projection along fiber axis calculated as described above (Fig. 4) for a double-wall cylinder with 18 Å inner radius and 28 Å outer radius. The constant for the hexagonal lattice was 69.4 Å. The skeletal atomic model indicates seven molecules at the inner radius, and 11 molecules at the outer. The lysine and tyrosine residues are arranged as above. The *R*-factor was 0.39. (*Right*) View along radial direction of an individual double-wall tube, shown at approximately twice the size. The depth of image was adjusted to clearly show the stacking of the foreground molecules in the fibril direction.

AcTR4 fibril assembly

The diffraction pattern from solubilized/dried AcTR4 clearly showed a fanning of the equatorial scattering, and Bragg peaks that superimposed on the diffuse scattering (Figs. 2 and 8, *left*). The angle of fanning was $2\alpha = 10°$, where α is the angle between the off-equatorial reflection and the equator. For a helical structure of radius r, and pitch P, the helical tilt $\beta = \pi/2 - \alpha$ can be expressed as $\beta = a\tan(P/2\pi r)$. From the measured angle (5°), and the 20 Å-fibril radius (see below), the helix pitch P was estimated as 1436 Å, which is comparable to the observed pitch for PHF (9).

The coherent domain size along the intersheet direction was calculated from the equatorial diffuse scattering at ~10 Å spacing (Fig. 8, *middle*), and found to correspond to the size of a pair of β-sheets separated by ~10 Å. Unlike the other peptide assemblies, the length of the polypeptide chain comprising a β-strand could not be clearly ascertained for AcTR4, since there was not an unambiguous minimum *R*-factor. The diffuse scattering on the equator was sampled by $(\sim 30\ \text{Å})^{-1}$, suggesting that there are two pair of double lines separated by ~33 Å (= ~30 × 1.11). Although the positions of the calculated intensity minima at 0.05 Å^{-1}, 0.15 Å^{-1}, and 0.25 Å^{-1} agreed with the observed ones, the

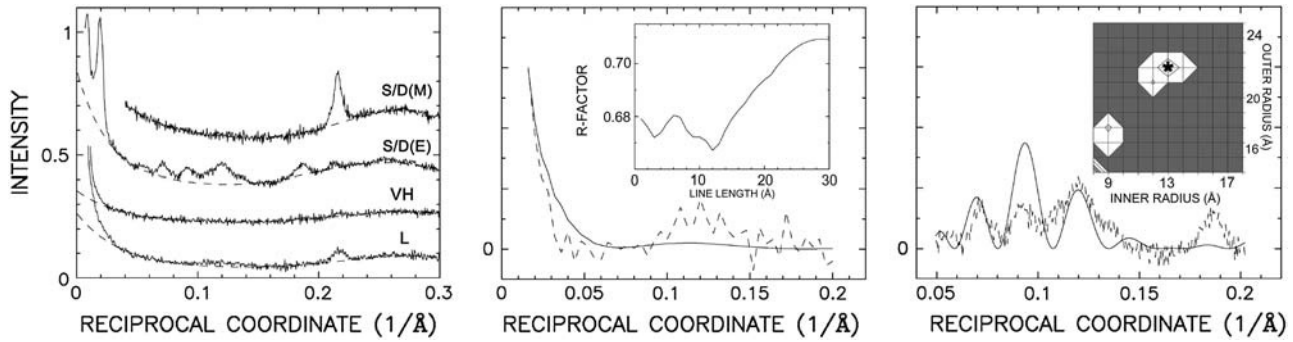

FIGURE 7 Analysis of x-ray diffraction from PHF/tau hexapeptide AcVQIVYK (AcPHF6). (*Left*) The intensity distribution along meridian of solubilized/dried (*S*/*D*(*M*)), equator of solubilized/dried (*S*/*D*(*E*)), vapor-hydrated (*VH*), and lyophilized (*L*) preparations. See preceding figure legends for details. (*Middle*) The observed intensity after background subtraction (*dashed*), and calculated intensity (*solid*) for lyophilized AcPHF6. The calculated curve was based on a model consisting of a pair of 12 Å-long lines separated by 8.3 Å. Normalization and LP correction as described above. (*Inset*) Dependence of *R*-factor on line length shows minimum at 12 Å. (*Right*) The observed (*dashed*) and calculated (*solid*) intensity distributions for solubilized/dried AcPHF6. The calculated intensity is based on a coaxial cylinder with walls at radii of 13 Å and 22 Å, and arrayed in a hexagonal lattice (107.3 Å unit cell constant). (*Inset*) Dependence of *R*-factor on different inner and outer radii (see above). A minimum *R*-factor of 0.68 was found as indicated by asterisk. (The boundary including the minimum was in the range of 0.65–0.70, and the subsequent boundaries were drawn at every 0.05.)

calculated intensities of the second and third intensity maxima at 0.2 $Å^{-1}$ and 0.3 $Å^{-1}$ were larger than the observed ones. Using the phase combinations of the model—i.e., $+-\ +-$ for the four loops—and the observed structure amplitudes, a one-dimensional electron density distribution was calculated (Fig. 8, *right*). This showed that the thickness of the plate was ~4 Å. In the future, defining such a step function model by multiple parameters may yet better fit the observed intensity.

DISCUSSION

Molecular structure of core domain and interaction between tau motifs PHF6 and PHF6*

X-ray diffraction patterns from the assemblies formed by the core domains AcVYK, AcPHF4, and AcPHF6 all showed that the structural unit is a coaxial (or double-wall) cylinder, and that the homotypic interactions between units varied according to the particular peptide and its physical state—i.e., lyophilized or hydrated. In the lyophilized AcVYK and AcPHF4, there was no intensity maxima signaling interference between the units, whereas in the solubilized/dried samples, the unit structures formed a hexagonal lattice. For the solubilized/dried AcPHF6 peptide, the lattice was disordered, so that the first two reflections corresponded to the interference peaks and the wide-angle reflections corresponded to the Fourier-transform of the double-wall cylinder. For the considerably longer peptide, AcTR4, a pair of β-sheets rather than the coaxial cylinder was the structural unit. In the core peptides, therefore, the cylindrical assembly may be stabilized by intermolecular interactions involving the N- and C-terminal moieties of the β-sheets; however, this

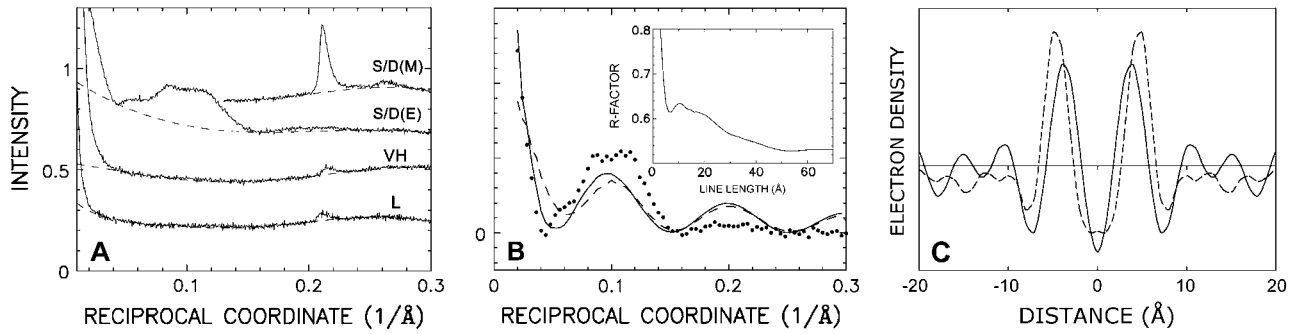

FIGURE 8 Analysis of x-ray diffraction from PHF/tau hexapeptide AcTR4. (*A*) The intensity distribution along meridian of solubilized/dried (*S*/*D*(*M*)), equator of solubilized/dried (*S*/*D*(*E*)), vapor-hydrated (*VH*), and lyophilized (*L*) preparations. See preceding figure legends for details. (*B*) The observed (after background subtraction, ●) and calculated (*solid* and *dashed lines*) intensity distributions for solubilized/dried AcTR4. The calculated ones are based on models consisting of a pair of 50 Å- (*solid*) or 10 Å-long (*dashed*) lines separated by 10 Å. (*Inset*) Dependence of *R*-factor on different line lengths with constant line separation 10 Å, showing a shallow minimum at 50 Å. (*C*) Relative electron density along the intersheet direction as a function of distance (Å) for lyophilized AcPHF6 (*solid line*), and for solubilized/dried AcTR4 (*dashed line*). The one-dimensional electron density $\rho(x)$ was calculated from the observed structure amplitudes $F_{amp}(h/d)$ according to $\rho(x) \propto \sum_h (\pm)|F_{amp}(h/d)|\cos(2\pi x h/d)$, where d was assumed to be 250 Å, and $\sum_h |F_{amp}(h/d)|^2/d = 0.03$. The phase from the model was either 0 or π.

interaction may be weaker for a longer peptide such as AcTR4. Our structure analysis and consideration of charge effects (see below) indicate that the tyrosine residues are likely localized in the intersheet space, whereas the lysine residues are located on the surface of the β-sheet facing the aqueous medium.

To account for the scattered x-ray intensity to ~5 Å spacing, we tested different models. Either a double-wall cylinder, or a double-line model were found to be consistent with the observed intensity. The size of four β-chains in the former and two in the latter agreed with our measurements of the coherent domain size from the integral width of the ~8–10 Å intersheet reflection.

In peptide AcTR4, there are two possible arrangements for the motif sequences PHF6 and PHF6*. Secondary structure prediction (19) indicated that these two sequences (VQIINK and VQIVYK) are in a β-conformation, and that the region between them is either turn or coil:

GKVQIINKLDLSNVQKDNIKHGSVQIVYKPVDLSKVT
tbbbbbbaaaabbbbtttccccbbbbbbbbccbbbbb

A turn between the motifs would create either an intersheet interaction or H-bonding between them. Because analysis of the shorter peptides indicates that the aromatic tyrosine residues are localized in the intersheet space, we propose that PHF6-PHF6 motifs likely interact together along the intersheet direction, whereas the PHF6 and PHF6*, also in the β-conformation, interact along the H-bonding direction. Polar zipper bonding between glutamine residues as indicated in polyglutamine structure (24,34) may also be involved in this H-bonding interaction.

Recent observation showed that Tyr-18 and Tyr-394 are phosphorylated (35). Because Tyr-18 is in the sequence HAGTYGL and Tyr-394 is in AEIVYKS, then these residues are not within the core sequences proposed to be involved in PHF formation. Whether these particular phosphorylated peptides are perhaps themselves amyloidogenic has not yet been determined.

Surface charge and kinetics

To test how the positions of ionizable groups in the fibril influences fibril formation by different tau peptides, we plotted the surface charge density (Table 3) as a function of the kinetic coefficients for fibril formation k_1, which were measured in the medium at pH 7.2 and ionic strength 0.15 (9). The surface charge density was determined from the molecular weight of the peptide, density, number of ionizable groups, and proton dissociation constant according to the Linderstrøm-Lang equation (36). The plot showed that the kinetic coefficient k_1 decreases exponentially with the surface charge density (Table 3, Fig. 9), indicating that larger surface charge slows fibril formation due to the greater electrostatic repulsion between proteins. For the peptides tested here, the charges arise only from the lysine residue at pH 7.2; therefore, this correlation confirms that lysine faces the aqueous medium as shown by the structural model.

Long-range interaction between β-sheets in macromolecular assembly

To what extent can the results obtained with lyophilized and solubilized/dried powder samples be taken to represent the behavior of the aggregate structures in aqueous solution (i.e., in the actual intracellular milieu)? The lyophilized sample for AcVYK and AcIVYK core domains showed tubular structures that were not ordered. After solubilization/drying the arrangement became ordered in a two-dimensional hexagonal lattice. Unlike these dried samples, the vapor-hydrated peptides showed a broader intersheet reflection likely due to the larger electrostatic repulsion between the tubular walls. In physiological medium at pH 7 and 0.15 ionic strength, the surface charge may be shielded by electrolytes (37,38). In water, this shielding is greatly reduced, such that the tubular structure may not be maintained.

Electrostatic effects on the separation between β-sheets may be evaluated according to the DLVO theory of colloid

TABLE 3 Surface charge density of PHF/tau peptides

Peptide	M	V (Å^3)	r (Å)	S (Å^2)	pI*	$\sigma \times 10^3$	K_1
AcYK	350	543	5.06	322	10.0	3.05	0.31
AcVYK	450	698	5.50	380	10.0	2.60	0.34
AcPHF4	563	873	5.93	442	10.0	2.24	2.64
AcPHF5	691	1071	6.35	506	10.0	1.96	3.19
AcPHF6	790	1225	6.64	554	10.0	1.79	8.54

The folding type, which was determined from the amino acid composition according to a multivariate method (18,96), showed irregular folding for all peptides. The hydrated volume of peptide [in Å^3] was calculated according to $V = M(\nu + \delta\nu_1)/N$, where M is the molecular weight, N is Avogadro number, ν is 0.73, $\delta = 0.2$, and $\nu_1 = 1$ (97). Therefore, V Å^3 = 1.55 M. Assuming a sphere for hydrated peptide having radius r [in Å], the surface area S [Å^2] is obtained from $S = 4\pi r^2$. Since polymerization was initiated by the addition of NaCl (to 0.15 M) at pH 7.2 (9), the ionic strength and pH of the medium were 0.15 and pH 7.2. The pI* tabulated in the Table was the pH value at which the charge density of the peptide was closest to zero, where we used intrinsic proton dissociation constants pK (98) for ionizable residues (N-, C-terminal residues were not considered), ionic strength 0.15, dielectric constant 80, and temperature 20°C, according to the Linderstrøm-Lang method (18,36,59). The radius b is that for the native protein, and is related to a which is the ion-exclusion radius according to $a = 2$ Å $+ b$. The radius a is assumed to be the same as the radius r. The ionizable residues included Asp, Glu, His, Tyr, Lys, and Arg, but not the N- and C-terminal moieties. A plot of the kinetic constant k_1 (9) as a function of the surface charge density which was calculated above for AcYK, AcVYK, AcPHF4, AcPHF5, and AcPHF6. k_1 decays exponentially with increase in the surface charge, indicating that electrostatic repulsion slows fibril formation. The trend line which fits best the observed points was $k_1 = 823 \exp(-2709\sigma)$ (see Fig. 9).

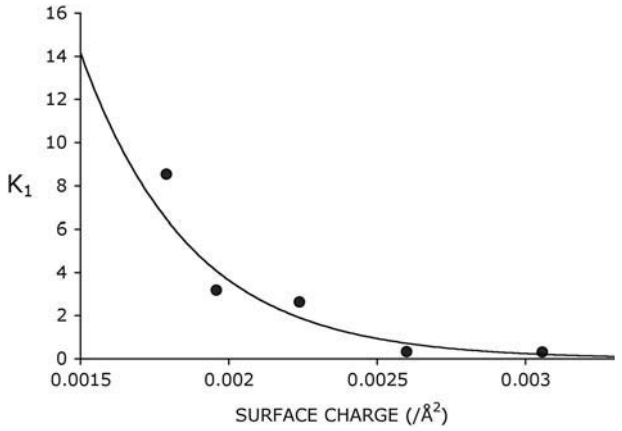

FIGURE 9 The rate constant K_1 (●) as a function of surface charge for different PHF peptides. The trend line (*solid*) is an exponential fit. See details in Table 3.

stability (37–40). In our study, the fixed surface charge density (σ) was determined by the chemical composition of the β-sheet, which is dependent on the proton dissociation constant and the local proton concentration. The surface charge of the β-sheet facing the external medium is

$$\sigma = eN/S,$$

where e is the elementary charge, and N is the number of fixed charges in surface area S. When there are ionizable groups A and B, the proton dissociation equilibrium is given by

$$HA \Leftrightarrow A^- + H^+$$
$$BH^+ \Leftrightarrow B + H^+.$$

The apparent proton dissociation constants K_a and K_b are described according to the mass action law,

$$K_a = [A^-][H^+]/[HA]$$
$$K_b = [B][H^+]/[BH^+],$$

where $[H^+]$ is the measured proton concentration of the bulk medium. The local concentration of $H^+(x)$ at position x is influenced by the electrostatic field $\phi(x)$ according to the Boltzmann distribution

$$[H^+(x)] = [H^+]\exp[-e\phi(x)/kT],$$

where $[H^+(x)]$ is the proton concentration at position x, k is the Boltzmann constant, and T is the absolute temperature. For an ionizable group at the surface, the apparent pK (= −logK) is related to the intrinsic pK (pK_{int}) by

$$pK = pK_{int} - e\phi(x_s)/(2.303kT).$$

Using the concentration of the ionizable groups A^- and BH^+, the surface charge density is

$$\sigma = (e/S)(-\sum_i [A_i^-] + \sum_j [BH_j^+]).$$

For an isolated sheet surface in the electrolyte medium, the surface charge is related to the electrostatic potential $\phi(x)$ according to

$$\sigma = \frac{\varepsilon kT}{2\pi e}\kappa \sinh[e\phi(x)/2kT],$$

where κ is the Debye parameter, ε is the dielectric constant of the medium, and n is the concentration of the univalent electrolyte (41). If there are two sheets separated by d_w at equilibrium, the separation can be determined by the balance of the electrostatic repulsion force F_r, hydration force, and the van der Waals attractive force F_a. The repulsion F_r is

$$F_r = 2nkT\{\cosh[2e\phi_1(d_w/2)/kT] - 1\}.$$

The potential at the center of the sheets is assumed to be twice that at position $d_w/2$ from the isolated charged surface. The factor $\phi_1(d_w/2)$ is determined by

$$\tanh[Y(d_w/2)/4] = \tanh[Y(x_s)/4]\exp(-\kappa(d_w/2))$$

and

$$\sigma = (\varepsilon kT/2\pi e)\kappa \sinh[Y(x_s)/2],$$

where

$$Y(x) = e\phi(x)/kT.$$

The attractive force F_a is given by

$$F_a = (H/6\pi)[1/d_w^3 - 2/(d_w + d_{ex})^3 + 1/(d_w + 2d_{ex})^3],$$

where d_w is the thickness of the water layer, and d_{ex} is the exclusion length, or thickness, of the plate.

Numerical calculation was performed as follows. The exclusion thickness of the tubular wall d_{ex} is ~20 Å, and d_w is the interplate water separation, which is similar to the inner diameter of the tube (28 Å and 36 Å for AcVYK and AcIVYK, respectively). Thus, the distance between the two plates is 48 Å and 56 Å. To evaluate the effect of ionic strength on the plate separation, we first determined the surface charge density at higher ionic strength, for example at $I = 0.3$ and pH 7. Assuming values for the Hamaker coefficient (5.0×10^{-14} erg) and the hydration force (1.93×10^{11} dyn/cm^2), and given that $d_{ex} = 20$ Å, then a 49 Å-separation between the two plates was determined when the surface charge was 1×10^{-3}/Å^2 and the voltage was 13 mV (Fig. 10 *A*). Using the same Hamaker coefficient, surface area, hydration force, temperature, and dielectric constant, the separation at $I = 0.15$ became 77 Å (Fig. 10 *B*). At $I = 0.01$, no equilibrium was observed. This calculation confirms that water disrupts the tubular structure due to a larger electrostatic repulsion force between lysine resides on β-sheets. This calculation also accounts for the shielding effect of electrolytes in physiological saline. If electrolytes bind to the lysine residues, then the tubular size may be further reduced.

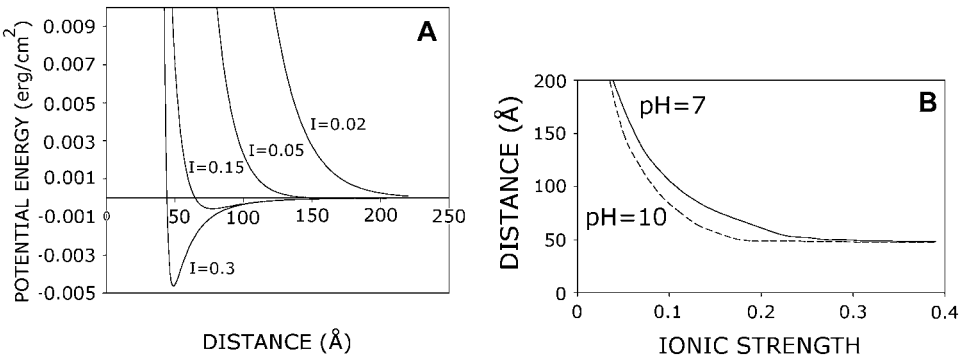

FIGURE 10 (*A*) Potential energy (erg/cm^2) as a function of distance between plates having one lysine reside per 1000 Å^2 of surface area at pH 7 at different ionic strength $I = 0.3$, 0.15, 0.05, and 0.02. Hamaker coefficient, 5.4×10^{-14} erg; hydration force, 1.93×10^{11} dyn/cm^2; temperature, 20°C; dielectric constant, 80; exclusion thickness of the plate, 20 Å; and the empirical surface area, A^2 per charge, were chosen. (*B*) Dependence of the distance between two plates at equilibrium as a function of ionic strength at pH 7 and pH 10. The parameters defining the model were the same as *A*.

Comparison with other x-ray studies of tau peptides

The first x-ray diffraction patterns from PHF aggregates purified from autopsy tissue (42) showed two reflections characteristic of the cross β-structure, i.e., 4.76 Å H-bonding distance and 10.6 Å intersheet distance. From the integral widths of the reflections, the coherent domain size of the structural unit or β-crystallite was estimated to be 80 Å for the H-bonding direction (along the fiber axis) and 40 Å for the intersheet direction (normal to the fiber axis). Tau peptide constructs K18 (7) and P301S (11), both of which contain four repeat domains, gave x-ray reflections, i.e., in the former, at 30 and 10.7 Å on the equator and 4.7 Å on the meridian, and in the latter at 13 Å on the equator and 4.7 Å on the meridian. The 4.7 Å reflection shows that the β-chains are periodic in the H-bonding direction for both peptides; and the equatorial ~10 Å reflection observed in construct K18 (7) arises from a β-sheet array in the intersheet direction. For construct P301S, which is a four-repeat tau, the authors did not account for the origin of the 13 Å-spacing reflection and did not report any ~10 Å reflection (11). However, inspection of their published pattern reveals a broad reflection at ~10 Å spacing (see Fig. 4 in (11)). Our estimate of the integral width of the 10 Å reflection for construct K18 (from Fig. 4 in (7)) is ~$(20 \text{ Å})^{-1}$, which corresponds to the size of a pair of β-sheets. If the low-angle reflection at ~30 Å in K18 arises from the first interference peak, a pair of sheets is, therefore, separated from another pair by ~33 Å after cylindrical averaging. This model for construct K18 is similar to the one proposed here for AcTR4 (see above).

Well-oriented x-ray diffraction patterns have been recorded from other PHF/tau peptides containing motif PHF6* (VQIINK): tau265-272 KYQIINKK, tau247–272, tau215–358, and four-repeat tau (4Rtau) (43). The short peptide tau265–272 gives equatorial and meridional reflections, which are ascribed to a one-dimensional lattices of periods 148 Å and 231.8 Å, respectively. As an apparent one-dimensional period on the equator in a cylindrically averaged fiber pattern should correspond to the intensity maxima of the J_0 Bessel term (20,44,45), then, the scattering object in the tau265–272 assembly would be a small crystallite having an interparticle distance of ~150 Å, which is comparable to the 120–150 Å-fibril size measured by EM (43). The authors indexed the meridional reflections at 4.79 Å, 4.73 Å, 4.65 Å, and 4.56 Å (near 4.7 Å) as layer lines 48, 49, 50, and 51. From the argument (43) that the structure is a helical array having a 14.69° twist for each β-strand, where the helical rule is written as $l = 2n + 49m$, where l, n, and m are integer, the period c is 232 Å, the pitch P is 116 Å, and the rise per unit h is 4.73 Å. The Bessel terms n for the cited layer lines, therefore, must be 24, 0, 25, and 1. Such a helical array deviates slightly from the helix giving ~15° twist for each β-strand, as earlier proposed (29). For the latter array, the helix rule may be $l = n + 24m$, $c = P = 115.5$ Å, and $h = 4.8$ Å for a coaxial cylinder having a 6.5 Å inner radius, and 16.5 Å outer radius (46). This type of helical array gives layer lines every $1/c$ in the fiber direction, which is not seen in the observed diffraction from tau265–272. Alternatively, therefore, these meridional and equatorial reflections may be indexed by a hexagonal lattice of unit cell $a = 4.79$ Å, $b = c = 57$ Å, and $\alpha = 120°$, where the a-axis is the H-bonding fiber direction. The hexagonal lattice constant normal to the H-bonding direction is similar to the size of the assemblies formed by peptides AcVYK, AcIVYK, and AcVQIVYK analyzed by x-ray diffraction in this article, and to the size of protofilaments observed by EM (Fig. 4 *A* in (43)). It may be that intersheet, homotypic tyrosine-tyrosine interactions are involved in peptide KYQIINKK assembly similar to what we concluded here for AcVYK.

The diffraction pattern for four-repeat tau peptide (43) gave remarkable crystalline diffraction. The authors indicated that tilted β-chains account for some reflections, but the Miller indices were not presented. In our preliminary interpretation of their pattern, we propose that the reflections may be indexed by an orthogonal unit cell of $a = 9.4$ Å, and $b = 12.72$ Å, where the a and b axes are in the directions of H-bonding and polypeptide chain. Given that the (110) direction on the equator is a fiber axis, the major reflections at 7.56 Å, 4.70 Å, 4.26 Å, 3.78 Å, and 3.04 Å are indexed as (110), (200), (030), (220), and (140), respectively. In this indexing, the angle between the respective reflection and the

equator is estimated to be 36° for the (200), 54° for the (030), and 35° for the (140), which account for the positions of the observed reflections. The β-chain tilt in this assembly is similar to the one found in AcTR4 (this study), and in Aβ1–40 (31,47), both of which give a twisted ribbonlike morphology. This observation supports the notion that β-chain tilt and morphology of twisting are correlated.

Core domain as a drug target

Studies on a series of Aβ analogs by electron microscopy and x-ray diffraction demonstrate that there is a short peptide core domain in Alzheimer's β-amyloid (20,30,42,48). Our current and previous study on tau protein analogs (9) showed that only a three-residue β-strand may be involved in nucleating fibril formation. This agrees with other findings that local interactions via H-bonding or aromatic residues between short peptides (49,50) are involved in amyloid formation—e.g., VYK for tau/PHF (9), LVFF for Aβ amyloid (21,51), NFGSVQ for medin (52), and DFNKF for calcitonin (53). Because flanking regions containing charged residues do not hinder the formation of β-sheet structures in polyalanine and polyglutamine peptides (24,54), it is likely that H-bonding between the peptide backbone and side chains may initiate β-sheet formation as a prelude to amyloid assembly.

Under different conditions, short peptides—e.g., Aβ fragments—can assemble into different assemblies, such as protofilament, fibril, or sheet (20,55). This indicates that the core domain is always involved in β-sheet formation, whereas the flanking regions are involved in the interaction between the β-crystallites. One current controversy (24) is whether such core domains in the full sequence are formed by parallel or antiparallel β-sheets.

Targeting local interactions is a reasonable approach to interfering with the initial nucleation of amyloid fibrils or to destroying the fibril once formed, as demonstrated by the use of an antibody against the local sequence or of a peptide analog to mimic the local structure—e.g., for Aβ (56,57) and for prion protein (58). Most small molecules, which have been shown to inhibit amyloid fibril formation in vitro, contain aromatic rings. Such inhibitors include Congo red (59,60) for Alzheimer's β-amyloid; anthraquinone (15); porphyrin (16) for tau; and anthracycline for prion (61). Our current study on the structure of the core peptides of PHF/tau indicates a possible tyrosine-tyrosine interaction, which suggests that the inhibitors may bind to aromatic residues in amyloid via π–π interaction (62). As in vitro studies typically use electron microscopy and fluorescent dyes to measure inhibitory effects, it is not clear to which state of assembly the drugs bind—i.e., whether to monomer, oligomer, protofilament, fibril, or even to cofactors such as heparin for tau fibril formation, or whether drugs influence the pH and ionic strength of the medium, which also could modulate amyloid assembly. It is of interest, therefore, to test whether and in

TABLE 4 Peptide nanotubular structures indicated by x-ray diffraction

Peptide	Assembly along fiber axis	Size	Characteristics	Possible application	Crystal data	Ref.
Aminocyclohexane carboxylic acid (Fig. 11 *A*)	H-bonding between cyclic β-chains	8 Å	Side chains face inner and outer medium	Ion channel	$a = 15.0485$ Å, $b = 13.7200$ Å, $c = 58.019$ Å, $\alpha = 90°$, $\beta = 91.672°$, $\gamma = 90°$ (I_2)	(84)
Phe-Phe (Fig. 11 *B*)	Phe side-chain interaction without H-bonding	13 Å	Both side chains face outside of the tube	Nanowire fabrication and membrane bound ion channel	$a = b = 24.071$ Å, $c = 5.456$ Å, $\alpha = \beta = 90°$, $\gamma = 120°$ ($P6_1$)	(81,88,99)
Val-Val (Fig. 11 *C*)	Helical	15 Å	Val residues face both sides	Nanowire fabrication and membrane bound ion channel	$a = b = 14.647$ Å, $c = 10.277$ Å, $\alpha = \beta = 90°$, $\gamma = 120°$ ($P6_1$)	(87)
Polyglutamine and Aβ1–40 (Fig. 11 *D*)	H-bonding between β-chains	20 Å	Side chains face both sides			(60,93)
Betabellin 15D (Fig. 11 *E*)	Helical array of β-sheets	20 Å	Rodlike structure			(23,94)
AcPHF3 (AcVYK) (Fig. 11 *F*)	H-bonding between bilayered β-chains	28 Å	Aromatic residues maintain bilayer 7 molecules at 14 Å 9 molecules at 21 Å			Current
AcPHF4 (AcIVYK) (Fig. 11 *G*)	H-bonding between bilayered β-chains	36 Å	Aromatic residues maintain bilayer 7 molecules at 18 Å 11 molecules at 28 Å			Current

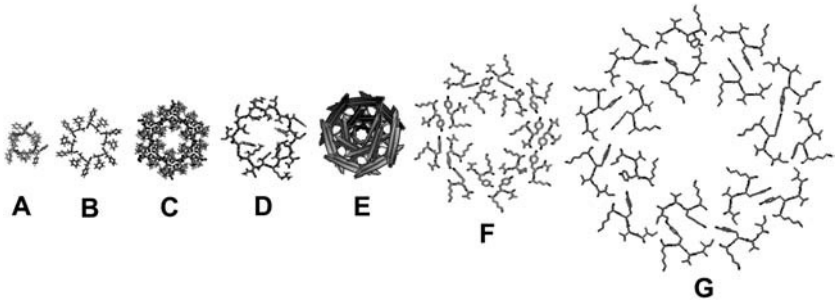

FIGURE 11 Cross-section views of peptide nanotube models. (*A*) Aminocyclohexane carboxylic acid (84), (*B*) diphenylalanine (88), (*C*) divaline (87), (*D*) Aβ1–40 nanotube (60), (*E*) betabellin 15D (23), (*F*) AcVYK (current study), and (*G*) AcIVYK (this study). The atomic coordinates were displayed by RASMOL (28) after correcting for any inappropriate stereochemistry using SwissViewer (25). The betabellin 15D structure was displayed using MOLSCRIPT (26). Further details of these models are summarized in Table 4.

what manner the drugs in fact bind to the protein. The illuminating method of wide-angle solution scattering, discussed recently (63), may be of particular value for this purpose.

Fibril morphology: twist and sheet

PHF/tau shows both a twisted ribbon structure having Gaussian curvature (64) and also straight, smooth cylindrical fibrils (3). Image analysis indicates that the heterogeneity may arise from a different assembly of constituent structural units (3). The distinct fibril morphology with twisting has been replicated by the equimolar mixing of two short peptides, VYK and PHF6 (9). Our current x-ray diffraction study shows that the AcVYK, AcPHF4, and AcPHF6 domains form straight cylindrical tubes where the peptide molecules in a β-chain conformation and running normal to the fiber axis constitute the tubular walls, whereas peptide AcTR4, which contains two different motif sequences, gave tilted and twisted β-chains. These observations, along with that on four-repeat tau (43), indicate that β-chain tilt may correlate with the twisted morphology of the fibril.

Two different fibril morphologies have also been observed for Aβ1–40, in the same batch and even in the same sample visible on the EM grid (31). Previously, we suggested that the fibril twist arises from the tilt of the β-chain in the amphipathic residues 22–35 in Aβ, since twisting fibrils were only observed for a limited number of amphipathic Aβ analogs including Aβ1–40 (33) and shorter peptides near the hydrophobic C-terminus, e.g., Aβ34–42, Aβ22–35, and Aβ25–35 (48,65,66).

Transformation from a twisted to a straight fiber can be experimentally induced, e.g., PHF fibers treated with NaOH (67), Aβ34–42 peptide treated with a denaturing agent (66), and Aβ1–40 peptides exposed to high pH (33). These findings suggest that both electrostatic and hydrophobic effects can influence the tilt or twist of the β-chains. Different morphologies were recently induced with Aβ1–40 by preparing quiescent or agitated fibrils (68). Thus, the β-strands in twisted fibrils (prepared under quiescent conditions) were found to reside in residue sequences 10–14, 16–22, 30–32, and 34–36, whereas β-strands in straight fibrils (prepared by agitation) reside in residue sequences 10–22, 30–32, and 34–36. These findings, which did not mention β-chain tilt, do suggest, however, that a difference in β-chain length may also be involved in fibril morphology. That distinctive morphologies can be transmitted to daughter fibrils (68), similar to what has been shown for the N-terminal domain of prion (69), suggests that the strain type in the latter may arise from protein conformation.

Twist morphology in macromolecular assemblies is not restricted to the protein aggregation state. A correlation between chain tilt and fibril twist is suggested also for lipids (70,71). Sphingomyelin causes lamellar lipid membranes to curve (72), and by itself forms a tubular structure in Gaucher's disease (73–75). Protein can also influence the curvature of lipid membranes—e.g., an 18-mer amphipathic peptide induces spherical liposomes to form Golgi-like nanotubular structures (76–78), and dynamin and amphiphysin can transform spherical liposomes into narrow tubules (79,80). Thus, regulation of chain tilt may be a crucial step in fabricating different types of macromolecular assemblies from proteins and lipids.

Peptide-based nanotubes

Our current x-ray study showed that short peptides can assemble as nanotubular structures that are coaxial cylinders, i.e., consisting of double walls. Peptide nanotubes are being investigated for possible engineering and medical applications including nanowire fabrication (81,82), angiogenesis and biointerface (83). Based on their molecular structure, the peptide nanotubes that have been previously described can be classified into six different types:

1. Cyclic (84–86)
2. VA-type dipeptide (87)
3. FF-type dipeptide (88)
4. β-helical (32,89)
5. Twisted β-ribbon (90)
6. Empty tube with β-chain in radial direction (91,92).

The VA-type includes dipeptides AL, LA, VV, VL, LV, AV, and the FF-type includes LL, LF, FL, IL, and WG. Single crystal x-ray diffraction has provided atomic details only for types *1–3*. The first peptide nanotubes were prepared from circular peptides composed of alternating *D*- and *L*-amino acids, such that all side chains face the same

direction when the peptide assumes a β-strand conformation (Fig. 11 *A*). In forming nanotubes, the cyclic peptides stack normal to the β-chain direction via H-bonding. For the VV dipeptide (type-*2* nanotube), the projection along the fiber direction shows a double helix (Fig. 11 *C*) with the hydrophobic side chains facing both inward toward the central pore and outward. For the FF dipeptide (type-*3* nanotube), which forms a single-wall tube (Fig. 11 *B*), the side chains face toward the outside of the pore, and the pore is surrounded by hydrophilic moieties. Van der Waals interactions between side chains, and not the H-bonding between peptides, stabilize the stacking of FF dipeptide monomers along the fiber axis. A β-helical nanotube (type *4*) was first proposed for polyglutamine (93), and a similar nanotube can be built from Aβ1–40 (32,60) (Fig. 11 *D*). A solid tubular structure was observed for the helical assembly of betabellin 15D (23,94). This structure is similar to the fibril observed for transthyretin amyloid (46,95). In our current analysis of the PHF/tau tri- and tetrapeptide nanotubes assembled from AcVYK (Fig. 11 *F*) and AcIVYK (Fig. 11 *G*), the 4.8 Å-pitch of the β-helix is like that of the postulated polyglutamine structure (93), but the number of residues per pitch varies for the different peptides. The bilayered β-helix assembly may be driven by aromatic interactions between β-sheets, with the bordering, charged (lysine) side chains likely facing the hydrophilic medium. This unique bilayered assembly, which we propose as a seventh type of nanotubular structure, may be useful as a template for developing specific ion-selection devices.

We thank the anonymous reviewers for their helpful comments concerning the issues related to crystallinity and electrostatic effects on peptide assembly, and Dr. Carl Henrik Görbitz for providing us with atomic coordinates of the peptides diphenylalanine and divaline.

The research was supported by an Alzheimer's Association/T.L.L. Temple Foundation Discovery Award (to D.A.K.), institutional support from Boston College, and National Institutes of Health-National Institute on Aging research grant No. 1R03AG16042-01 (to W.J.G.).

REFERENCES

1. Hodge, A. J., and W. J. Adelman Jr. 1983. The neuroplasmic lattice, structural characteristics in vertebrate and invertebrate axons. *In* Structure and Function in Excitable Cells. D. C. Chang, I. Tasaki, W. J. Adelman Jr., and H. R. Leuchtage, editors. Plenum Press. New York. 75–111.
2. Brandt, R. 1996. The tau proteins in neuronal growth and development. *Front. Biosci.* 1:d118–d130.
3. Crowther, R. A. 1991. Straight and paired helical filaments in Alzheimer disease have a common structural unit. *Proc. Natl. Acad. Sci. USA.* 88:2288–2292.
4. Alonso, A., T. Zaidi, M. Novak, I. Grundke-Iqbal, and K. Iqbal. 2001. Hyperphosphorylation induces self-assembly of tau into tangles of paired helical filaments/straight filaments. *Proc. Natl. Acad. Sci. USA.* 98:6923–6928.
5. Necula, M., and J. Kuret. 2004. Pseudophosphorylation and glycation of tau protein enhance but do not trigger fibrillization in vitro. *J. Biol. Chem.* 279:49694–49703.
6. Schneider, A., J. Biernat, M. von Bergen, E. Mandelkow, and E. M. Mandelkow. 1999. Phosphorylation that detaches tau protein from microtubules (Ser-262, Ser-214) also protects it against aggregation into Alzheimer paired helical filaments. *Biochemistry.* 38:3549–3558.
7. von Bergen, M., S. Barghorn, L. Li, A. Marx, J. Biernat, E. M. Mandelkow, and E. Mandelkow. 2001. Mutations of tau protein in frontotemporal dementia promote aggregation of paired helical filaments by enhancing local β-structure. *J. Biol. Chem.* 276:48165–48174.
8. von Bergen, M., P. Friedhoff, J. Biernat, J. Heberle, E. M. Mandelkow, and E. Mandelkow. 2000. Assembly of tau protein into Alzheimer paired helical filaments depends on a local sequence motif (^{306}VQIVYK^{311}) forming β structure. *Proc. Natl. Acad. Sci. USA.* 97:5129–5134.
9. Goux, W. J., L. Kopplin, A. D. Nguyen, K. Leak, M. Rutkofsky, V. D. Shanmuganandam, D. Sharma, H. Inouye, and D. A. Kirschner. 2004. The formation of straight and twisted filaments from short tau peptides. *J. Biol. Chem.* 279:26868–26875.
10. von Bergen, M., S. Barghorn, J. Biernat, E. M. Mandelkow, and E. Mandelkow. 2005. Tau aggregation is driven by a transition from random coil to β-sheet structure. *Biochim. Biophys. Acta.* 1739: 158–166.
11. Berriman, J., L. C. Serpell, K. A. Oberg, A. L. Fink, M. Goedert, and R. A. Crowther. 2003. Tau filaments from human brain and from in vitro assembly of recombinant protein show cross-β structure. *Proc. Natl. Acad. Sci. USA.* 100:9034–9038.
12. Margittai, M., and R. Langen. 2004. Template-assisted filament growth by parallel stacking of tau. *Proc. Natl. Acad. Sci. USA.* 101:10278–10283.
13. Sadqi, M., F. Hernandez, U. Pan, M. Perez, M. D. Schaeberle, J. Avila, and V. Munoz. 2002. α-Helix structure in Alzheimer's disease aggregates of tau-protein. *Biochemistry.* 41:7150–7155.
14. Goux, W. J. 2002. The conformations of filamentous and soluble tau associated with Alzheimer paired helical filaments. *Biochemistry.* 41: 13798–13806.
15. Pickhardt, M., Z. Gazova, M. von Bergen, I. Khlistunova, Y. Wang, A. Hascher, E. M. Mandelkow, J. Biernat, and E. Mandelkow. 2005. Anthraquinones inhibit tau aggregation and dissolve Alzheimer's paired helical filaments in vitro and in cells. *J. Biol. Chem.* 280:3628–3635.
16. Taniguchi, S., N. Suzuki, M. Masuda, S. Hisanaga, T. Iwatsubo, M. Goedert, and M. Hasegawa. 2005. Inhibition of heparin-induced tau filament formation by phenothiazines, polyphenols, and porphyrins. *J. Biol. Chem.* 280:7614–7623.
17. Smith, T. F., and M. S. Waterman. 1981. Identification of common molecular subsequences. *J. Mol. Biol.* 147:195–197.
18. Inouye, H., and D. A. Kirschner. 1991. Folding and function of the myelin proteins from primary sequence data. *J. Neurosci. Res.* 28:1–17.
19. Garnier, J., D. J. Osguthorpe, and B. Robson. 1978. Analysis of the accuracy and implications of simple methods for predicting the secondary structure of globular proteins. *J. Mol. Biol.* 120:97–120.
20. Inouye, H., P. E. Fraser, and D. A. Kirschner. 1993. Structure of β-crystallite assemblies formed by Alzheimer β-amyloid protein analogues: analysis by x-ray diffraction. *Biophys. J.* 64:502–519.
21. Inouye, H., and D. A. Kirschner. 1996. Refined fibril structures: the hydrophobic core in Alzheimer's amyloid β-protein and prion as revealed by x-ray diffraction. *Ciba Found. Symp.* 199:22–35.
22. Inouye, H., and D. A. Kirschner. 1997. X-ray diffraction analysis of scrapie prion: intermediate and folded structures in a peptide containing two putative α-helices. *J. Mol. Biol.* 268:375–389.
23. Inouye, H., J. E. Bond, S. P. Deverin, A. Lim, C. E. Costello, and D. A. Kirschner. 2002. Molecular organization of amyloid protofilament-like assembly of betabellin 15D: helical array of β-sandwiches. *Biophys. J.* 83:1716–1727.
24. Sharma, D., L. M. Shinchuk, H. Inouye, R. Wetzel, and D. A. Kirschner. 2005. Polyglutamine homopolymers having 8–45 residues form slab-like β-crystallite assemblies. *Proteins Struct. Funct. Bioinform.* 61:398–411.
25. Guex, N., A. Diemand, and M. C. Peitsch. 1999. Protein modelling for all. *Trends Biochem. Sci.* 24:364–367.
26. Kraulis, P. J. 1991. MOLSCRIPT: a program to produce both detailed and schematic plots of protein structures. *J. Appl. Crystallogr.* 24:946–950.

27. McRee, D. E. 1999. XtalView/Xfit—a versatile program for manipulating atomic coordinates and electron density. *J. Struct. Biol.* 125: 156–165.
28. Sayle, R. A., and E. J. Milner-White. 1995. RASMOL: biomolecular graphics for all. *Trends Biochem. Sci.* 20:374–376.
29. Blake, C., and L. Serpell. 1996. Synchrotron x-ray studies suggest that the core of the transthyretin amyloid fibril is a continuous β-sheet helix. *Structure.* 4:989–998.
30. Kirschner, D. A., H. Inouye, L. K. Duffy, A. Sinclair, M. Lind, and D. J. Selkoe. 1987. Synthetic peptide homologous to β-protein from Alzheimer disease forms amyloid-like fibrils in vitro. *Proc. Natl. Acad. Sci. USA.* 84:6953–6957.
31. Malinchik, S. B., H. Inouye, K. E. Szumowski, and D. A. Kirschner. 1998. Structural analysis of Alzheimer's β(1–40) amyloid: protofilament assembly of tubular fibrils. *Biophys. J.* 74:537–545.
32. Perutz, M. F., J. T. Finch, J. Berriman, and A. Lesk. 2002. Amyloid fibers are water-filled nanotubes. *Proc. Natl. Acad. Sci. USA.* 99:5591–5595.
33. Fraser, P. E., J. T. Nguyen, H. Inouye, W. K. Surewicz, D. J. Selkoe, M. B. Podlisny, and D. A. Kirschner. 1992. Fibril formation by primate, rodent, and Dutch-hemorrhagic analogues of Alzheimer amyloid β-protein. *Biochemistry.* 31:10716–10723.
34. Perutz, M. F., T. Johnson, M. Suzuki, and J. T. Finch. 1994. Glutamine repeats as polar zippers: their possible role in inherited neurodegenerative diseases. *Proc. Natl. Acad. Sci. USA.* 91:5355–5358.
35. Derkinderen, P., T. M. E. Scales, D. P. Hanger, K. Y. Leung, H. L. Byers, M. A. Ward, C. Lenz, C. Price, I. N. Bird, T. Perera, S. Kellie, R. Williamson, W. Noble, R. A. Van Etten, K. Leroy, J. P. Brion, C. H. Reynolds, and B. H. Anderton. 2005. Tyrosine 394 is phosphorylated in Alzheimer's paired helical filament tau and in fetal tau with c-Abl as the candidate tyrosine kinase. *J. Neurosci.* 25:6584–6593.
36. Tanford, C., and R. Roxby. 1972. Interpretation of protein titration curves. Application to lysozyme. *Biochemistry.* 11:2192–2198.
37. Inouye, H., and D. A. Kirschner. 1988. Membrane interactions in nerve myelin. II. Determination of surface charge from biochemical data. *Biophys. J.* 53:247–260.
38. Inouye, H., and D. A. Kirschner. 1988. Membrane interactions in nerve myelin. I. Determination of surface charge from effects of pH and ionic strength on period. *Biophys. J.* 53:235–245.
39. Inouye, H., H. Tsuruta, J. Sedzik, K. Uyemura, and D. A. Kirschner. 1999. Tetrameric assembly of full-sequence protein zero myelin glycoprotein by synchrotron x-ray scattering. *Biophys. J.* 76:423–437.
40. Ninham, B. W., and V. A. Parsegian. 1971. Electrostatic potential between surfaces bearing ionizable groups in ionic equilibrium with physiologic saline solution. *J. Theor. Biol.* 31:405–428.
41. Verwey, E. J. W., and J. Th. G. Overbeek. 1948. Theory of the Stability of Lyophobic Colloids. Elsevier, New York.
42. Kirschner, D. A., C. Abraham, and D. J. Selkoe. 1986. X-ray diffraction from intraneuronal paired helical filaments and extraneuronal amyloid fibers in Alzheimer disease indicates cross-β conformation. *Proc. Natl. Acad. Sci. USA.* 83:503–507 [published erratum appears in *Proc. Natl. Acad. Sci. USA*, 83:2776].
43. Giannetti, A. M., G. Lindwall, M. F. Chau, M. J. Radeke, S. C. Feinstein, and L. A. Kohlstaedt. 2000. Fibers of tau fragments, but not full length tau, exhibit a cross β-structure: implications for the formation of paired helical filaments. *Protein Sci.* 9:2427–2435.
44. Burge, R. E. 1961. The structure of bacterial flagella: the packing of the polypeptide chains within a flagellum. *Proc Roy Soc (Lond.).* A260:558–573.
45. Vainshtein, B. K. 1966. Diffraction of X-Rays by Chain Molecules. Elsevier, New York.
46. Inouye, H., F. S. Domingues, A. M. Damas, M. J. Saraiva, E. Lundgren, O. Sandgren, and D. A. Kirschner. 1998. Analysis of x-ray diffraction patterns from amyloid of biopsied vitreous humor and kidney of transthyretin (TTR) Met-30 familial amyloidotic polyneuropathy (FAP) patients: axially arrayed TTR monomers constitute the protofilament. *Amyloid.* 5:163–174.
47. Fraser, P. E., J. T. Nguyen, D. T. Chin, and D. A. Kirschner. 1992. Effects of sulfate ions on Alzheimer β/A4 peptide assemblies: implications for amyloid fibril-proteoglycan interactions. *J. Neurochem.* 59:1531–1540.
48. Fraser, P. E., L. K. Duffy, M. B. O'Malley, J. Nguyen, H. Inouye, and D. A. Kirschner. 1991. Morphology and antibody recognition of synthetic β-amyloid peptides. *J. Neurosci. Res.* 28:474–485.
49. Gazit, E. 2002. A possible role for π-stacking in the self-assembly of amyloid fibrils. *FASEB J.* 16:77–83.
50. Makin, O. S., E. Atkins, P. Sikorski, J. Johansson, and L. C. Serpell. 2005. Molecular basis for amyloid fibril formation and stability. *Proc. Natl. Acad. Sci. USA.* 102:315–320.
51. Tjernberg, L., W. Hosia, N. Bark, J. Thyberg, and J. Johansson. 2002. Charge attraction and β propensity are necessary for amyloid fibril formation from tetrapeptides. *J. Biol. Chem.* 277:43243–43246.
52. Reches, M., and E. Gazit. 2004. Amyloidogenic hexapeptide fragment of medin: homology to functional islet amyloid polypeptide fragments. *Amyloid.* 11:81–89.
53. Reches, M., Y. Porat, and E. Gazit. 2002. Amyloid fibril formation by pentapeptide and tetrapeptide fragments of human calcitonin. *J. Biol. Chem.* 277:35475–35480.
54. Shinchuk, L. M., D. Sharma, S. E. Blondelle, N. Reixach, H. Inouye, and D. A. Kirschner. 2005. Poly-(L-alanine) expansions form core β-sheets that nucleate amyloid assembly. *Proteins Struct. Funct. Bioinform.* 61:579–589.
55. Fraser, P. E., J. T. Nguyen, W. K. Surewicz, and D. A. Kirschner. 1991. pH-dependent structural transitions of Alzheimer amyloid peptides. *Biophys. J.* 60:1190–1201.
56. Soto, C., E. M. Sigurdsson, L. Morelli, R. A. Kumar, E. M. Castano, and B. Frangione. 1998. β-sheet breaker peptides inhibit fibrillogenesis in a rat brain model of amyloidosis: implications for Alzheimer's therapy. *Nat. Med.* 4:822–826.
57. Tjernberg, L. O., J. Naslund, F. Lindqvist, J. Johansson, A. R. Karlstrom, J. Thyberg, L. Terenius, and C. Nordstedt. 1996. Arrest of β-amyloid fibril formation by a pentapeptide ligand. *J. Biol. Chem.* 271:8545–8548.
58. Chabry, J., B. Caughey, and B. Chesebro. 1998. Specific inhibition of in vitro formation of protease-resistant prion protein by synthetic peptides. *J. Biol. Chem.* 273:13203–13207.
59. Inouye, H., and D. A. Kirschner. 2000. Aβ fibrillogenesis: kinetic parameters for fibril formation from Congo red binding. *J. Struct. Biol.* 130:123–129.
60. Inouye, H., and D. A. Kirschner. 2005. Alzheimer's β-amyloid: insights into fibril formation and structure from Congo red binding. *Subcell. Biochem.* 38:203–224.
61. Tagliavini, F., R. A. McArthur, B. Canciani, G. Giaccone, M. Porro, M. Bugiani, P. M. J. Lievens, O. Bugiani, E. Peri, P. Dall'Ara, M. Rocchi, G. Poli, G. Forloni, T. Bandiera, M. Varasi, A. Suarato, P. Cassutti, M. A. Cervini, J. Lansen, M. Salmona, and C. Post. 1997. Effectiveness of anthracycline against experimental prion disease in Syrian hamsters. *Science.* 276:1119–1122.
62. Hunter, C. A., and J. K. M. Sanders. 1990. The nature of $\pi-\pi$ interactions. *J. Am. Chem. Soc.* 112:5525–5534.
63. Fischetti, R. F., D. J. Rodi, D. B. Gore, and L. Makowski. 2004. Wide-angle x-ray solution scattering as a probe of ligand-induced conformational changes in proteins. *Chem. Biol.* 11:1431–1443.
64. Selinger, R. L. B., J. V. Selinger, A. P. Malanoski, and J. M. Schnur. 2004. Shape selection in chiral self-assembly. *Phys. Rev. Lett.* 93: 158103.
65. Fraser, P. E., J. T. Nguyen, D. R. McLachlan, C. R. Abraham, and D. A. Kirschner. 1993. α1-antichymotrypsin binding to Alzheimer Aβ-peptides is sequence-specific and induces fibril disaggregation in vitro. *J. Neurochem.* 61:298–305.
66. Halverson, K., P. E. Fraser, D. A. Kirschner, and P. T. Lansbury, Jr. 1990. Molecular determinants of amyloid deposition in Alzheimer's disease: conformational studies of synthetic β-protein fragments. *Biochemistry.* 29:2639–2644.

67. Wischik, C. M., R. A. Crowther, M. Stewart, and M. Roth. 1985. Subunit structure of paired helical filaments in Alzheimer's disease. *J. Cell Biol.* 100:1905–1912.

68. Petkova, A. T., R. D. Leapman, Z. H. Guo, W. M. Yau, M. P. Mattson, and R. Tycko. 2005. Self-propagating, molecular-level polymorphism in Alzheimer's β-amyloid fibrils. *Science.* 307:262–265.

69. Jones, E. M., and W. K. Surewicz. 2005. Fibril conformation as the basis of species- and strain-dependent seeding specificity of mammalian prion amyloids. *Cell.* 121:63–72.

70. Chung, D. S., G. B. Benedek, F. M. Konikoff, and J. M. Donovan. 1993. Elastic free energy of anisotropic helical ribbons as metastable intermediates in the crystallization of cholesterol. *Proc. Natl. Acad. Sci. USA.* 90:11341–11345.

71. Zastavker, Y. V., N. Asherie, A. Lomakin, J. Pande, J. M. Donovan, J. M. Schnur, and G. B. Benedek. 1999. Self-assembly of helical ribbons. *Proc. Natl. Acad. Sci. USA.* 96:7883–7887.

72. Curatolo, W., and L. J. Neuringer. 1986. The effects of cerebrosides on model membrane shape. *J. Biol. Chem.* 261:17177–17182.

73. Kulkarni, V. S., J. M. Boggs, and R. E. Brown. 1999. Modulation of nanotube formation by structural modifications of sphingolipids. *Biophys. J.* 77:319–330.

74. Lee, R. E., C. R. Worthington, and R. H. Glew. 1973. The bilayer nature of deposits occurring in Gaucher's disease. *Arch. Biochem. Biophys.* 159:259–266.

75. Yunis, E. J., and R. E. Lee. 1970. Tubules of globoid leukodystrophy: a right-handed helix. *Science.* 169:64–66.

76. Furuya, T., T. Kiyota, S. Lee, T. Inoue, G. Sugihara, A. Logvinova, P. Goldsmith, and H. M. Ellerby. 2003. Nanotubules formed by highly hydrophobic amphiphilic α-helical peptides and natural phospholipids. *Biophys. J.* 84:1950–1959.

77. Kitamura, A., T. Kiyota, M. Tomohiro, A. Umeda, S. Lee, T. Inoue, and G. Sugihara. 1999. Morphological behavior of acidic and neutral liposomes induced by basic amphiphilic α-helical peptides with systematically varied hydrophobic-hydrophilic balance. *Biophys. J.* 76:1457–1468.

78. Lee, S., T. Furuya, T. Kiyota, N. Takami, K. Murata, Y. Niidome, D. E. Bredesen, H. M. Ellerby, and G. Sugihara. 2001. De novo-designed peptide transforms Golgi-specific lipids into Golgi-like nanotubules. *J. Biol. Chem.* 276:41224–41228.

79. Sweitzer, S. M., and J. E. Hinshaw. 1998. Dynamin undergoes a GTP-dependent conformational change causing vesiculation. *Cell.* 93: 1021–1029.

80. Takei, K., V. I. Slepnev, V. Haucke, and P. De Camilli. 1999. Functional partnership between amphiphysin and dynamin in clathrin-mediated endocytosis. *Nat. Cell Biol.* 1:33–39.

81. Reches, M., and E. Gazit. 2003. Casting metal nanowires within discrete self-assembled peptide nanotubes. *Science.* 300:625–627.

82. Scheibel, T., R. Parthasarathy, G. Sawicki, X. M. Lin, H. Jaeger, and S. L. Lindquist. 2003. Conducting nanowires built by controlled self-assembly of amyloid fibers and selective metal deposition. *Proc. Natl. Acad. Sci. USA.* 100:4527–4532.

83. Narmoneva, D. A., O. Oni, A. L. Sieminski, S. Zhang, J. P. Gertler, R. D. Kamm, and R. T. Lee. 2005. Self-assembling short oligopeptides and the promotion of angiogenesis. *Biomaterials.* 26:4837–4846.

84. Amorin, M., L. Castedo, and J. R. Granja. 2003. New cyclic peptide assemblies with hydrophobic cavities: the structural and thermodynamic basis of a new class of peptide nanotubes. *J. Am. Chem. Soc.* 125:2844–2845.

85. Hartgerink, J. D., J. R. Granja, R. A. Milligan, and M. R. Ghadiri. 1996. Self-assembling peptide nanotubes. *J. Am. Chem. Soc.* 118:43–50.

86. Horne, W. S., C. D. Stout, and M. R. Ghadiri. 2003. A heterocyclic peptide nanotube. *J. Am. Chem. Soc.* 125:9372–9376.

87. Görbitz, C. H. 2003. Nanotubes from hydrophobic dipeptides: pore size regulation through side chain substitution. *New J. Chem.* 27: 1789–1793.

88. Görbitz, C. H. 2001. Nanotube formation by hydrophobic dipeptides. *Chemi. Eur. J.* 7:5153–5159.

89. Valery, C., M. Paternostre, B. Robert, T. Gulik-Krzywicki, T. Narayanan, J. C. Dedieu, G. Keller, M. L. Torres, R. Cherif-Cheikh, P. Calvo, and F. Artzner. 2003. Biomimetic organization: octapeptide self-assembly into nanotubes of viral capsid-like dimension. *Proc. Natl. Acad. Sci. USA.* 100:10258–10262.

90. Aggeli, A., G. Fytas, D. Vlassopoulos, T. C. B. McLeish, P. J. Mawer, and N. Boden. 2001. Structure and dynamics of self-assembling β-sheet peptide tapes by dynamic light scattering. *Biomacromolecules.* 2:378–388.

91. Lu, K., J. Jacob, P. Thiyagarajan, V. P. Conticello, and D. G. Lynn. 2003. Exploiting amyloid fibril lamination for nanotube self-assembly. *J. Am. Chem. Soc.* 125:6391–6393.

92. Vauthey, S., S. Santoso, H. Gong, N. Watson, and S. Zhang. 2002. Molecular self-assembly of surfactant-like peptides to form nanotubes and nanovesicles. *Proc. Natl. Acad. Sci. USA.* 99: 5355–5360.

93. Perutz, M. F., B. J. Pope, D. Owen, E. E. Wanker, and E. Scherzinger. 2002. Aggregation of proteins with expanded glutamine and alanine repeats of the glutamine-rich and asparagine-rich domains of Sup-35 and of the amyloid β-peptide of amyloid plaques. *Proc. Natl. Acad. Sci. USA.* 99:5596–5600.

94. Lim, A., A. M. Makhov, J. Bond, H. Inouye, L. H. Connors, J. D. Griffith, B. W. Erickson, D. A. Kirschner, and C. E. Costello. 2000. Betabellins 15D and 16D, de novo designed β-sandwich proteins that have amyloidogenic properties. *J. Struct. Biol.* 130:363–370.

95. Damas, A. M., and M. J. Saraiva. 2000. Review: TTR amyloidosis-structural features leading to protein aggregation and their implications on therapeutic strategies. *J. Struct. Biol.* 130:290–299.

96. Kubota, Y., S. Takahashi, K. Nishikawa, and T. Ooi. 1981. Homology in protein sequences expressed by correlation coefficients. *J. Theor. Biol.* 91:347–361.

97. Inouye, H., J. T. Nguyen, P. E. Fraser, L. M. Shinchuk, A. B. Packard, and D. A. Kirschner. 2000. Histidine residues underlie Congo red binding to Aβ-analogs. *Amyloid.* 7:179–188.

98. Nozaki, Y., and C. Tanford. 1967. Examination of titration behavior. *Methods Enzymol.* 11:715–734.

99. Song, T., S. R. Challa, C. J. Medforth, Y. Qiu, R. K. Watt, D. Pena, J. E. Miller, F. vanSwol, and J. A Shelnutt. 2004. Synthesis of peptide-nanotube platinum-nanoparticle composites. *Chem. Commun.* 1044–1045.

100. Merritt, E. A., and M. E. P. Murphy. 1994. Raster3D Version 2.0. A program for photorealistic molecular graphics. *Acta Crystallogr. D Biol. Crystallogr.* 50:869–873.